

An Interacting Galaxy System Along a Filament in a Void

B. Beygu¹, K. Kreckel², R. van de Weygaert¹, J. M. van der Hulst¹, J. H. van Gorkom³
 beygu@astro.rug.nl

ABSTRACT

Cosmological voids provide a unique environment for the study of galaxy formation and evolution. The galaxy population in their interior have significantly different properties than average field galaxies. As part of our Void Galaxy Survey (VGS), we have found a system of three interacting galaxies (VGS_31) inside a large void. VGS_31 is a small elongated group whose members are embedded in a common HI envelope. The HI picture suggests a filamentary structure with accretion of intergalactic cold gas from the filament onto the galaxies. We present deep optical and narrow band H α data, optical spectroscopy, near-UV and far-UV GALEX and CO(1-0) data. We find that one of the galaxies, a Markarian object, has a ring-like structure and a tail evident both in optical and HI. While all three galaxies form stars in their central parts, the tail and the ring of the Markarian object are devoid of star formation. We discuss these findings in terms of a gravitational interaction and ongoing growth of galaxies out of a filament. VGS_31 is one of the first observed examples of a filamentary structure in a void. It is an important prototype for understanding the formation of substructure in a void. This system also shows that the galaxy evolution in voids can be as dynamic as in high density environments.

Subject headings: galaxies: evolution — galaxies: formation — galaxies: kinematics and dynamics — galaxies: structure — large-scale structure of universe — radio lines: galaxies

1. Introduction

Voids are vast regions occupying most of the volume in the universe with sizes in the range of 20 - 50 h^{-1} Mpc, usually roundish in shape and largely devoid of galaxies (see [van de Weygaert & Platen 2011](#), for a recent review). In the large scale structure of the universe we observe today, the most striking features along with the voids are clusters and filaments. In this picture, galaxies are distributed in a filament-dominated web-like structure. Filaments connect clusters to each other and, while tenuous, act like bridges ([Zel'dovich 1970](#); [Shandarin & Zeldovich 1989](#); [Bond et al. 1996](#); [Colberg et al. 2005a](#); [Aragón-Calvo et al.](#)

[2010b](#)). From recent redshift surveys like the second Center for Astrophysics Redshift Survey ([Davis et al. 1983](#)), the 2dF Galaxy Redshift Survey ([Colless et al. 2003](#)), the Sloan Digital Sky Survey (SDSS) ([York et al. 2000](#)) and 2MASS redshift survey ([Huchra et al. 2012](#)) we see how filaments, bridges and sheet-like structures form substructures and surround the underdense regions.

Notwithstanding the very low density of the void regions, we do find a dilute population of galaxies in their interior. These *void galaxies* appear to have significantly different properties than average field galaxies. Previous studies based on redshift surveys, have shown that the void galaxies are in general small, star forming blue galaxies. They have a later morphological type and have higher specific star formation rates than the galaxies in average density environment. Largely unaffected by the complexities and processes modifying galaxies in high-density environments, the galaxies living in the isolated void regions are ex-

¹Kapteyn Astronomical Institute, University of Groningen, PO Box 800, 9700 AV Groningen, the Netherlands

²Max Planck Institute for Astronomy, Königstuhl 17, 69117 Heidelberg, Germany

³Department of Astronomy, Columbia University, Mail Code 5246, 550 West 120th Street, New York, NY 10027, USA

pected to have retained vital clues to their formation and evolution. It has made the study of the relation between void galaxies and their surroundings an important aspect of the recent interest in environmental influences on galaxy formation (Szomoru et al. 1996; Kuhn et al. 1997; Popescu et al. 1997; Karachentseva et al. 1999; Grogin & Geller 1999, 2000; Peebles 2001; Hoyle & Vogeley 2002; Hoyle et al. 2002; Rojas et al. 2004, 2005; Tikhonov & Karachentsev 2006; Patiri et al. 2006a,b; Ceccarelli et al. 2006; Wegner & Grogin 2008; Stanonik et al. 2009; Kreckel et al. 2011, 2012).

Void galaxies may be the rare probes of the faint and tenuous substructure that hierarchical structure formation theories predict to exist in voids (Dubinski et al. 1993; van de Weygaert & van Kampen 1993; Sahni et al. 1994; Sheth & van de Weygaert 2004; Furlanetto & Piran 2006; Einasto et al. 2011; Aragón-Calvo & Szalay 2013). Cosmological simulations show how voids are filled by low-density dark matter filaments, creating a network of tenuous substructures within their interior (van de Weygaert & van Kampen 1993; Gottlöber et al. 2003; Colberg et al. 2005b; Springel et al. 2006). This may indicate that the galaxies residing in voids are formed along these dark matter filaments, given that the simulations reveal that dark matter haloes are forming along them. In fact, some earlier observational studies have found indications for such filamentary substructure in voids (Szomoru et al. 1996; Zitrin & Brosch 2008). For example, the latter argue that the dwarf galaxies in their local galaxy sample are located on a dark matter filament that itself is located in a low galaxy density region and is accreting intergalactic cold gas onto the filament.

In this study, we present the most outstanding example of such a filamentary void galaxy configuration, VGS_31, which was found within the context of the “Void Galaxy Survey” (VGS) (Kreckel et al. 2011, 2012).

We are conducting a multiwavelength survey of 60 void galaxies, called “The Void Galaxy Survey” (VGS) (Kreckel et al. 2011). Galaxies in the VGS have been selected from the Sloan Digital Sky Survey Data Release 7 (SDSS DR7) using purely geometric and topological techniques. The sample was selected on the basis of galaxy density maps produced by the Delaunay Tessellation Field Esti-

mator (DTFE, Schaap & van de Weygaert (2000); van de Weygaert & Schaap (2009)) and the subsequent application of the Watershed Void Finder (WVF, Platen et al. (2007); for a more general application of the watershed transform to the structural analysis of the cosmic web see Aragón-Calvo et al. (2010a). The combination of DTFE maps with WVF detected voids allow us to identify the void galaxies from the deepest interior regions of identified voids in the SDSS redshift survey. The goal of this survey is to study the galaxy properties in the most underdense and most pristine environments in the universe where the evolution of galaxies is expected to progress more slowly and relatively undisturbed.

Our geometrically selected sample consist of small galaxies, with stellar mass less than $3 \times 10^{10} M_{\odot}$. Most of these are small, blue star forming disk galaxies and many of them have companions and extended HI disks, which are often morphologically and kinematically disturbed (Kreckel et al. 2011, 2012).

We have found a system of three linearly aligned galaxies, VGS_31, in a void as part of the VGS (Figure 1 and 2). A remarkable feature of VGS_31 is that the whole system is embedded in a common HI envelope (Figure 3) and the three galaxies are at almost the same velocity (Figure 4). The fact that there is a small velocity gradient throughout whole HI envelope, from the far east of VGS_31b to far west to VGS_31c, suggests that this is a filament in which the three galaxies are embedded.

The system exhibits strong signs of interactions (Figure 1) and star forming activity with signs of starbursts (Figure 5 and 6). VGS_31 consists of a central galaxy VGS_31a and two companions; VGS_31b and VGS_31c. VGS_31a is optically slightly disturbed. It has a bar like structure and all the star formation activity is concentrated there. VGS_31b is a Markarian galaxy (Mrk 1477). Markarian galaxies are known to have UV continuum excess in their spectra. They have relatively high star formation rates and many of them contain AGNs and starburst nuclei. They span a wide luminosity range between -23 and -13 mag and have a broad range of morphologies. One interesting statistic is that an unusual number of Markarian galaxies occur in tight pairs or interacting systems. In this context, VGS_31b is a typ-

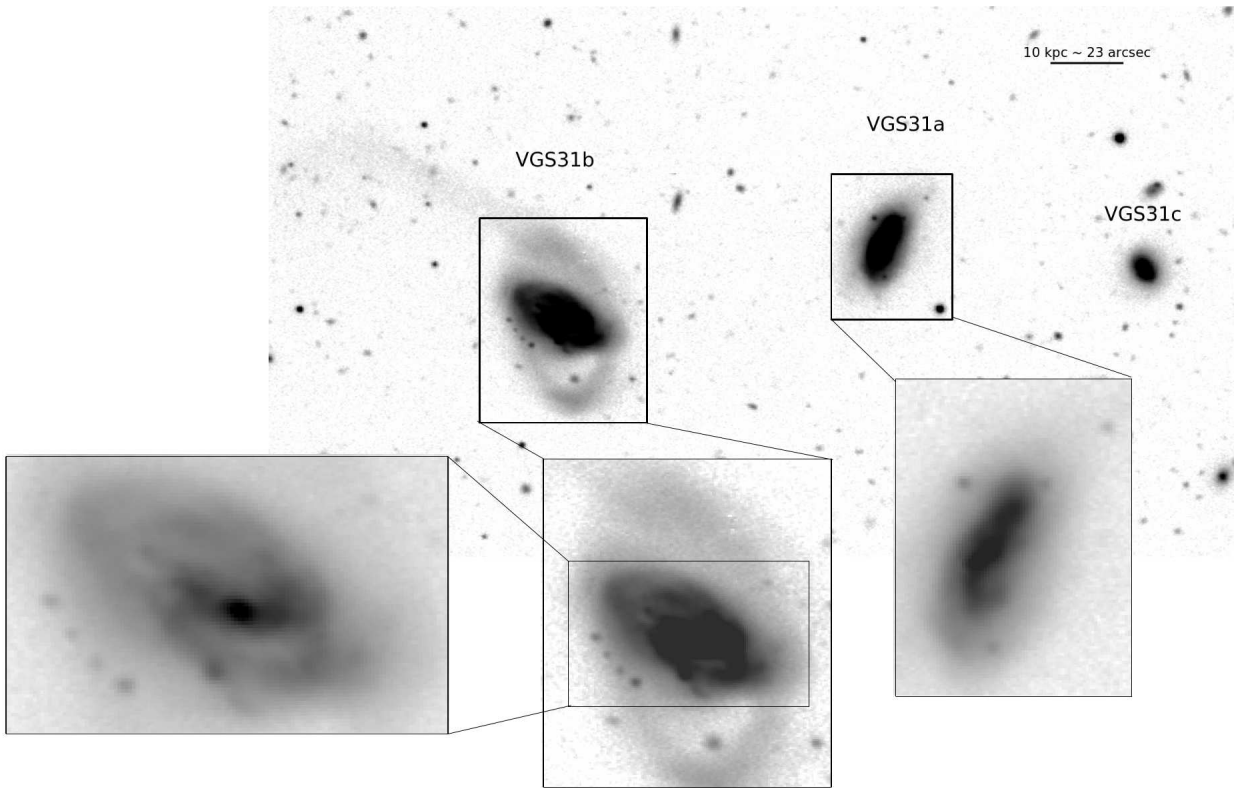


Fig. 1.— R band negative image of VGS_31. From left to right: *VGS_31b*: The most remarkable member of the system, a *Markarian* galaxy, has a tail and a ring. Close up images show the inner structures such as the bar. *VGS_31a*: A disk galaxy with a bar structure. *VGS_31c*: Smallest member of the system is optically undisturbed. The black bar on the top-right corner represents 10 kpc ($\sim 23''$).

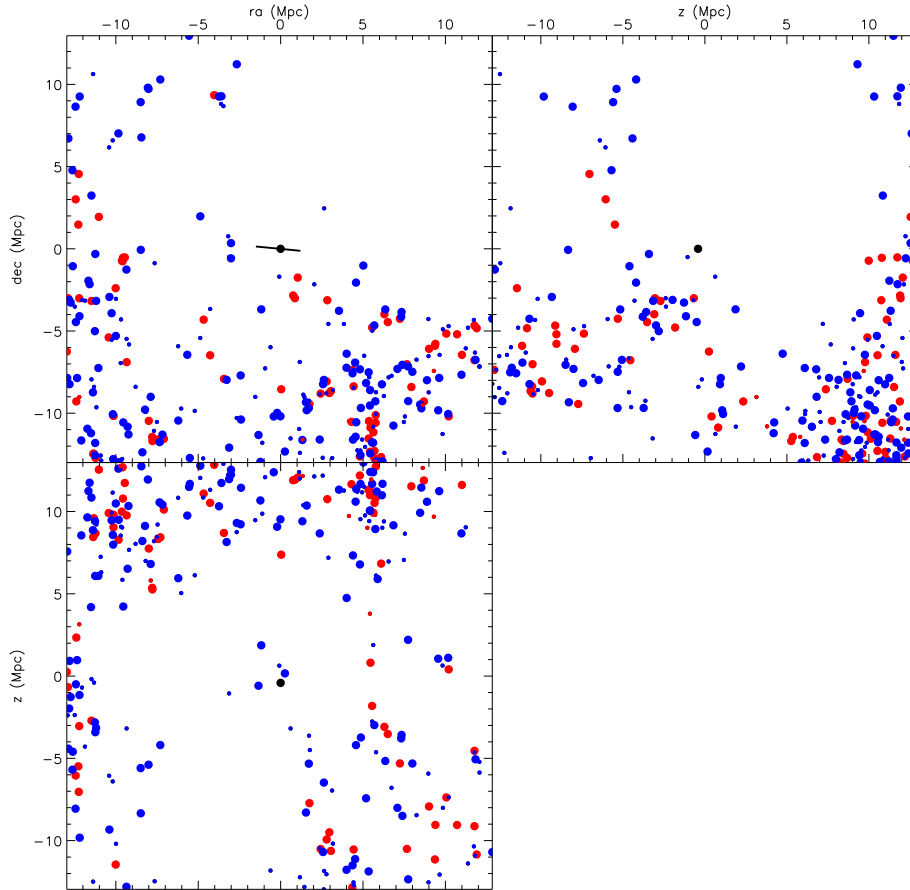


Fig. 2.— The large scale structure distribution of galaxies within 13 Mpc around the VGS_31 system (in black) for different projections in right ascension, declination, and redshift space. The line indicates the orientation of the system on the plane of the sky. Surrounding galaxies are color coded by $g-r$ color, to be red if $g-r > 0.6$ and blue if $g-r \leq 0.6$. The symbol size indicates luminosity, with larger symbols if $M_r < -18$ and smaller symbols if $M_r \geq -18$.

ical example of Markarian galaxy. VGS_31b is a starburst galaxy and has enhanced star formation at center of the disk mostly concentrated in the bar. It has a tail, visible both in optical and in HI and a ring like structure around the disk. There is no sign for ongoing star formation activity neither in the tail nor in the ring (Figure 5). VGS_31c is significantly smaller than the other two galaxies and forms stars in its central part as well.

At first glance VGS_31 looks like a normal interacting system. However the observed properties described above indicate a more complex picture as we may be witnessing the growth of structure along a filament within a large cosmological void. In fact, in an accompanying paper by Rieder et al. 2013 (subm.) we have explored the dynamical evolution of the growth of systems resembling VGS_31 in voids, within the context of the Λ CDM cosmology. In this study we analysed the high-resolution Λ CDM simulation Cosmo-Grid (Portegies Zwart et al. 2010) to see how dark matter halo systems similar in mass, size and environment to VGS_31 came to be. We found eight systems as suitable candidates for harbouring a VGS_31 like system and then investigated their merger histories. We found that while VGS_31-like systems have a large variation in formation time, the environment in which they are embedded evolved very similarly. It seems to suggest that we may be witnessing the assembly of a filament in a void by bringing together several smaller filamentary structures, each populated by individual haloes. It conjures up the interesting question whether the galaxies in the VGS_31 configuration were formed at the same location or whether they each originate from a different location.

In order to study the current properties and assembly history of the VGS_31 system in detail, we have obtained a multiwavelength data set. To investigate the low surface brightness features, we performed deep B and R band imaging, and to derive star formation properties and star formation history we have used deep H_α and UV imaging. Gas morphology, kinematics and molecular hydrogen content have been investigated using 21cm HI and CO observations.

This paper is organized as follows: Section 2 describes the observations, data analysis and the derivation of star formation properties for VGS_31. Section 3 gives the main observational

results such as star formation rate (SFR) properties, gas content and the morphology. In Section 4 we discuss the results. Finally, in Section 5 we speculate on the nature and the importance of VGS_31.

2. Observations and Data Reduction

VGS_31 has been observed in several wavelengths with various telescopes between 2009 and 2012. B & R band imaging has been gathered with the Isaac Newton Telescope (INT) at La Palma using the Wide Field Camera (WFC). Long slit spectra were obtained at the William Herschel Telescope (WHT) using the Intermediate dispersion Spectrograph and Imaging System (ISIS). Narrow band H_α imaging has been done using the Hiltner Telescope at the Michigan-Dartmouth-MIT Observatory (MDM). Near UV (NUV) and far UV (FUV) images have been taken from the Nearby Galaxy Atlas (NGA) of GALEX. Radio observations in the 21cm HI line were performed with the Westerbork Synthesis Radio Telescope (WSRT) and CO(1-0) emission spectra have been obtained with IRAM. A summary of the observational studies is given in Table 1. Parameters, quantitative results such as SFRs, HI and molecular hydrogen and stellar masses are presented in Table 2, Table 3, Table 4 and Table 5, respectively.

2.1. HI imaging

We have imaged the HI in VGS_31 as part of the VGS project, the details of which are described in Kreckel et al. (2012). Observations were done with the Westerbork Synthesis Radio Telescope (WSRT) in the maxi-short configuration providing an angular resolution of $19'' \times 32''$. The $36'$ full width half maximum of the WSRT primary beam is sufficient to cover the entire VGS_31 sys-

Table 1: Observing summary for VGS_31

Telescope	Observation details
INT	B & R band imaging
MDM 2.4m	H_α imaging
WHT	Long slit spectrum
WSRT	21cm (HI) imaging
IRAM	CO(1-0) observations
GALEX	NUV & FUV imaging

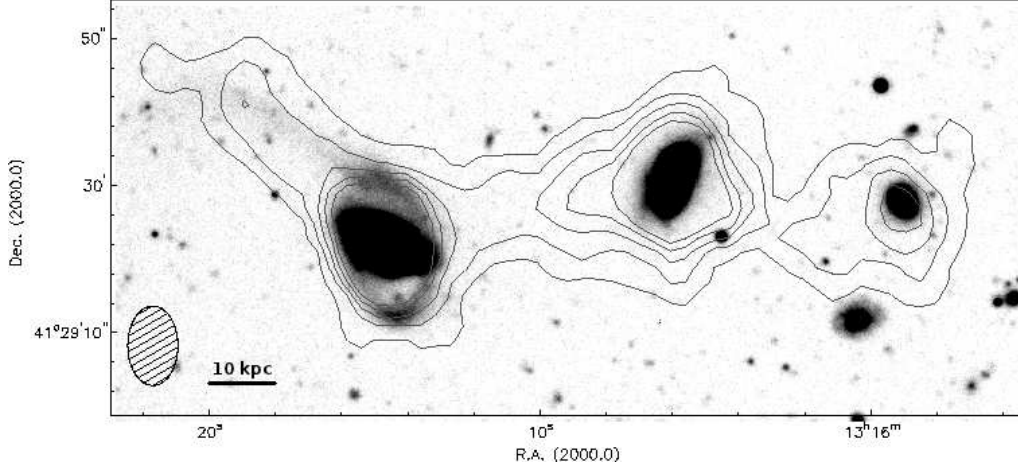


Fig. 3.— The HI intensity map of VGS31. HI column density intensity contours start at $1.6 \times 10^{19} \text{cm}^{-2}$ and increase with $4 \times 10^{19} \text{cm}^{-2}$ increments. Note that members of VGS_31 are aligned along a HI filament and appear to be embedded in a common HI envelope.

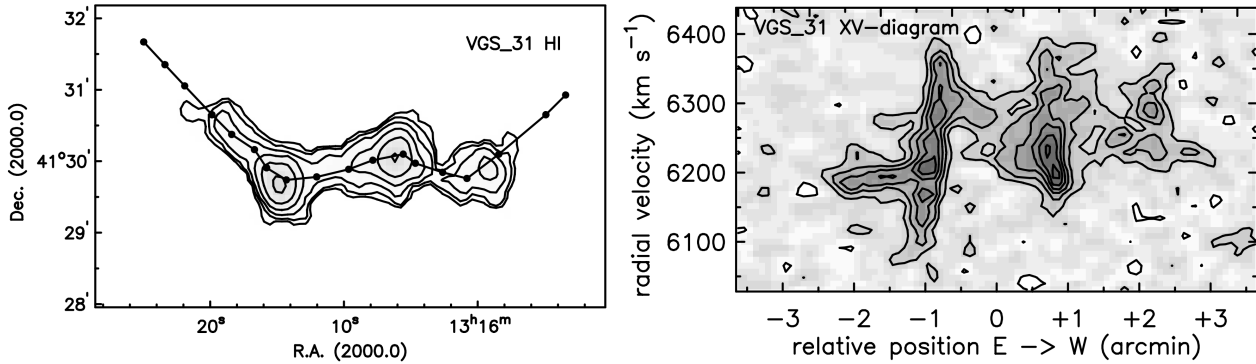


Fig. 4.— Position velocity (PV) diagram of VGS.31. Left: Slice position. The black line on the total HI map indicates the position of the slice used to create the position velocity (PV) diagram. Black cross is the the zero point (RA: 13:16:10). Right: PV diagram. The PV diagram is created by taking a slice along the whole HI structure, from the beginning of the tail to the end of VGS.31c, connecting each points. Zero corresponds to the red dot in the HI image on the left. This plot shows the velocity structure of the tail and its connection to gas around VGS.31b. Also, it shows the gas between VGS.31b and VGS.31a and VGS.31a and VGS.31c, respectively. Notice the change in velocity width between VGS.31b and VGS.31a.

TABLE 2
PARAMETERS FOR VGS_31

Name	SDSS ID	ra (J2000)	dec (J2000)	z	m_r	M_r	$g-r$	m_B	M_B	δ
VGS_31a	J131606.19+413004.2	13:16:06.19	+41:30:04.25	0.021	14.75	-20.01	0.32	14.633	-20.194	-0.64
VGS_31b	J131614.69+412940.0	13:16:14.69	+41:29:40.05	0.021	14.38	-20.38	0.50	14.632	-20.193	-0.64
VGS_31c	J131559.18+412955.9	13:15:59.18	+41:29:55.96	0.021	16.78	-17.98	0.21	16.735	-18.093	-0.64

NOTE.—Column 1: Galaxy names. Column 2: SDSS IDs of the galaxies. Column 3 & 4: Right ascensions and declinations. Column 5: Spectrophotometric redshifts. Column 6 & 7: Apparent and absolute r magnitudes drawn from the SDSS DR7 and corrected for galactic extinction. Column 8: $g-r$ colors drawn from the apparent model magnitudes as measured by the SDSS DR7. Column 9 & 10: Apparent and absolute B magnitudes derived from INT B band imaging and corrected for galactic extinction. Column 11: δ gives the filtered density contrast at $R_f = 1h^{-1}\text{Mpc}$ as described in [Kreckel et al. \(2011\)](#).

tem in a single pointing. We observed 512 channels within a total bandwidth of 10 MHz, giving a Hanning smoothed velocity resolution of 8.6 km s^{-1} . Images for this paper were made with natural weighting to maximize sensitivity and CLEANed down to $0.5 \text{ mJy beam}^{-1}$ ($\sim 1 \sigma$), reaching column density sensitivities of $2 \times 10^{19} \text{ cm}^{-2}$.

2.2. Broad band imaging and photometric calibration

We used the Wide Field Camera (WFC) at the 2.1m INT for imaging in both B and R bands with Harris B and R filters. Total exposure times were 2400 second for B and 1800 seconds for the R band, spread over 4 exposures for the purpose of dithering and facilitating cosmic ray detection. Standard star fields were observed each night for the photometric calibration. Flat field exposures were taken at twilight at the beginning and/or end of each night. The data have been reduced using the standard IRAF¹ and Photom Data Reduction Package (STARLINK)² procedures for CCD imaging. All the optical images were trimmed and overscanned followed by bias subtraction and flat fielding. After that all images from each filter were aligned and median combined. The same procedures have been followed for the standard star observations.

¹<http://iraf.noao.edu/>

²<http://star-www.rl.ac.uk/>

2.3. H_α imaging and photometric calibration

H_α imaging has been done with the Echelle CCD in direct mode at the 2.4 m Hiltner Telescope. A redshifted H_α filter centered at 6693 \AA has been used. To provide a measure of the continuum, R band imaging has been performed for each object. The total integration times for H_α and for the continuum have been spread over 3 exposures for the purpose of dithering and for facilitating cosmic ray detection. Spectrophotometric calibration stars have been chosen either from [Massey et al. \(1988\)](#) or [Oke \(1990\)](#).

After performing the standard CCD reduction steps described in section 2.1, each combined H_α image has been divided by 600 and R band continuum image by 120 in order to normalize them to 1 second. The mean has been calculated for an empty region in each image and the ratio of these means has been taken as the scaling factor for scaling the continuum image before subtraction from the H_α image. Photometric calibration of the final H_α images has been performed following the steps described in [Gavazzi et al. \(2006\)](#) and the references therein. Corrections for the atmospheric extinction and the airmass have been performed in the standard way, where each spectrophotometric calibration star observation has been fitted using airmass and instrumental magnitudes to get the atmospheric extinction coefficient.

Contribution of the $[N II]$ line to the observed flux has been estimated using the expression from

Kennicutt et al. (2008) and has been subtracted from the H_α flux.

Correction for the foreground extinction has been derived from Balmer decrements, following the recipes in Calzetti et al. (2000) and Domínguez et al. (2012). The H_α/H_β ratio ratios have been obtained from the MPA-JHU catalog for the SDSS DR7³ measured through 3'' fibers. We have calculated E(B-V) from these H_α/H_β ratios, using the reddening curve from Calzetti et al. (2000) to obtain the corresponding extinction. By using Balmer decrements we correct the foreground extinction along the entire line of sight including galactic extinction. Here an important point is that this correction assumes that the H_α/H_β ratio is the same throughout the entire H_α emission region. We checked this assumption using our WHT long slit spectra which measure the H_α/H_β ratios along slits which covers the emission along both the minor and the major optical axis. In Table 3, we give both the corrected and uncorrected H_α fluxes.

2.3.1. SFR from H_α imaging

Star formation rates (SFR) from the H_α emission have been calculated following the conversion from Kennicutt et al. (2009) where we used the SFR conversion factor based on a ‘‘Kroupa’’ initial mass function (Kroupa & Weidner 2003):

$$SFR(H_\alpha) [M_\odot yr^{-1}] = 5.4 \times 10^{-42} \times L(H_\alpha),$$

where $L(H_\alpha)$ is the luminosity, calculated as

$$L(H_\alpha) [erg s^{-1}] = 4 \pi D^2 (3.086 \times 10^{24})^2 I(H_\alpha),$$

where D is the distance to the galaxy in Mpc and $I(H_\alpha)$ is foreground extinction corrected flux.

A detailed description of the H_α photometry, foreground extinction correction and star formation derivation will be given in a separate paper.

2.4. Spectroscopy

We used the Intermediate dispersion Spectrograph and Imaging System (ISIS) at the 4.2 m WHT at La Palma to take high resolution spectra. The R1200R grating in the red arm and the

³The MPA-JHU catalog is publicly available and may be downloaded at <http://www.mpa-garching.mpg.de/SDSS/DR7/archive>

R600B grating in the blue arm have been used, giving resolutions of respectively 0.026 nm/pixel over 620-720 nm and 0.045 nm/pixel over 360-540 nm. CuNeAr lamp exposures were taken for wavelength calibrations. All the reduction has been performed using IRAF. In addition to the basic steps explained above, the illumination function along the slit has been determined via sky and lamp flats. Flux calibration has been done using spectrophotometric standard stars.

Figure 7 shows the H_α emission along the optical major and minor axis of VGS_31a and VGS_31b. In this figure, we compare the H_α emission line profiles with the H_α images of the corresponding regions on the galaxies.

2.5. GALEX UV observations

GALEX NUV and FUV data have been obtained from the Nearby Galaxy Atlas (NGA), taken in 2004 with an exposure time of 3754 seconds in the NUV and 3002 seconds in the FUV. VGS_31 falls as a background object in the corresponding science frame. The data was calibrated on the basis of the GALEX pipelines.

2.5.1. SFR from NUV

The SFR has been calculated from the GALEX NUV and FUV luminosities and corrected for internal dust attenuation following the method outlined in Schiminovich et al. (2010).

$$SFR = \frac{L_{UV} f_{UV}(young) 10^{0.4A_{UV}}}{\eta_{UV}},$$

where L_{UV} is the luminosity in $erg s^{-1} Hz^{-1}$, $f_{UV}(young)$ is the fraction of light that originates in young stellar populations, η_{UV} is the conversion factor between UV luminosity and recent-past-averaged star formation rate and A_{UV} is the dust attenuation.

To determine the values of A_{FUV} and A_{NUV} we assume $f_{UV}(young) = 1$ and $\eta_{UV} = 10^{28.165}$ (Schiminovich et al. 2010).

2.6. CO(1-0) emission line observations

CO(1-0) line observations have been carried out with the IRAM 30-m telescope at Pico Veleta, Spain in 2011. We used the Eight Mixer Receiver (EMIR) to observe simultaneously the CO(1-0)

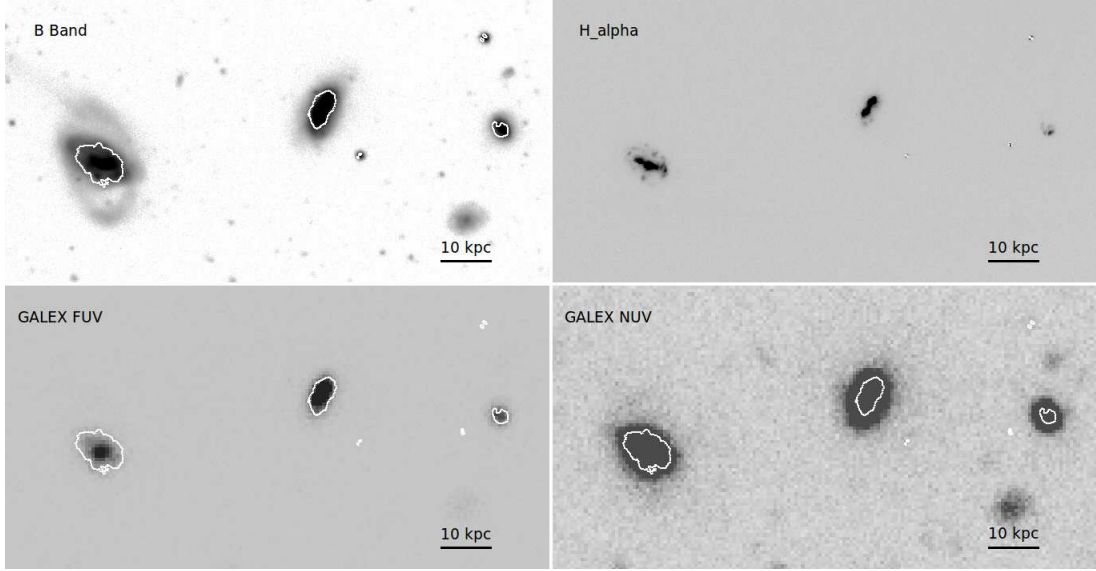


Fig. 5.— VGS_31 in four wavelength regimes. From top-left to bottom-right: a) INT B band image. b) MDM H_α continuum-subtracted image c) GALEX Far UV image, d) GALEX Near UV image. All the images are shown at the same physical scale. The white contours on each image indicate the corresponding H_α emission regions. Note that there is no H_α emission in the ring or in the tail of VGS_31b. Also note that the H_α emission is confined to the central parts of the galaxies, mostly in the bar structures of VGS_31a and VGS_31b.

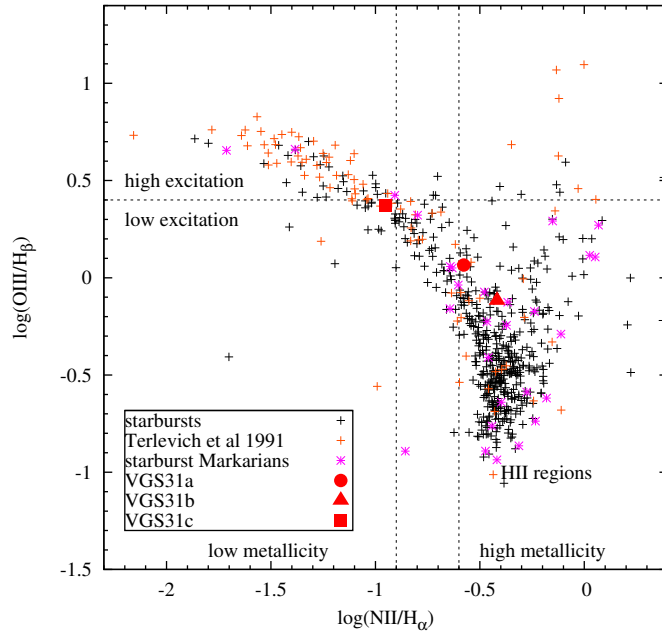


Fig. 6.— BPT diagram. The BPT diagram shows the ratio of emission line fluxes of $[O\ III]/H_\beta$ to $[N\ II]/H_\alpha$. The comparison sample of emission-line galaxies has been constructed from the emission-line galaxy sample of [Terlevich et al. \(1991\)](#), galaxies defined as starbursts in SIMBAD and Markarian galaxies defined as starbursts in [Coziol \(2003\)](#). This diagram is adapted from [Raimann et al. \(2000\)](#).

(rest frequency, 115.271 GHz) and the CO(2-1) emission line (rest frequency, 222.8118 GHz) with a resolution of 5km/s. The full width half maximum (FWHM) is, respectively, $\sim 22''$ and $\sim 11''$ at the two frequencies. The Wideband Line Multiple Autocorrelator (WILMA) and the Fast Fourier Transform Spectrometer (FTS) were used as backends. WILMA and FTS cover a channel width of 4 GHz with 2MHz and 195 KHz resolution, respectively. The observations were carried out in wobbler switching mode with a frequency of 1Hz and a throw of 120 $''$. The data were reduced with the CLASS software.

We have detected CO(1-0) emission from VGS.31b and the profile is shown in Figure 7. VGS.31b was not detected in CO(2-1). The detection limit for CO(2-1) is $\sim 1 K km s^{-1}$. This is consistent with a normal CO(1-0)/CO(2-1) ratio, provided the CO(2-1) emission is distributed over the CO(1-0) beam area.

The data for VGS.31a was not usable because of an error in the focus setting. VGS.31c has not been observed.

2.6.1. CO Luminosity and Mass

IRAM spectra are expressed in terms of antenna temperature (T_A^*). In order to convert it to a flux density we adopted the expressions following Costagliola et al. (2011) and Saintonge et al. (2011):

$$S_{CO}[Jy] = T_A^*[K] \times 3.906 \times \frac{F_{eff}}{\eta_A},$$

where F_{eff} is the forward efficiency and η_A is the antenna efficiency. The total flux is then derived by integrating the observed CO profile over velocity.

From the total flux we have calculated the luminosity as follows:

$$L'_{CO} = 3.25 \times 10^7 S_{CO} \nu_{obs}^{-2} D_L^2 (1+z)^{-3},$$

where L'_{CO} is the luminosity, ν_{obs} is the observed frequency in units of GHz, D_L is the luminosity distance in Mpc and z is redshift. Finally molecular hydrogen mass M_{H_2} is calculated as:

$$M_{H_2} = L'_{CO} \times \alpha_{CO},$$

where α_{CO} is the Galactic conversion factor of $3.2M_{\odot} [(K km sec^{-1} pc^2)^{-1}]$ which does not include a correction for the presence of Helium.

3. Results

Combining the data from the diverse set of observations presented in Section 2, the following picture on the nature of VGS.31 emerges.

VGS.31 consists of three galaxies located in a void, VGS.31a, b and c (Figure 1). A careful study of the HI properties suggests that the galaxies are embedded in an elongated HI cloud (Figure 3 and 4). In addition, both the optical and the HI observations suggest strong interactions in the system (Figure 3). This emerging picture tells us that we may be dealing with two different processes. One is the assembly of a filamentary structure in a void, the other is an interaction between the galaxies. We will describe these two main results separately.

VGS.31 exhibits a very peculiar structure in HI. The HI column density map and the position-velocity (PV) diagram (Figure 3 and 4) present two views elucidating the nature of the system; *i) the filamentary structure* and *ii) its kinematic properties*.

3.1. Filamentary structure

The PV diagram seen on the right hand side of Figure 4, is created by taking one single slice through the HI data cube, from the far east to the far west of the VGS.31. In the HI column density map (Figure 3) galaxies appear to be lined up in a HI filament. The whole HI envelope extends over ~ 120 kpc on the sky. The PV diagram shows that the three galaxies are at about the same systemic

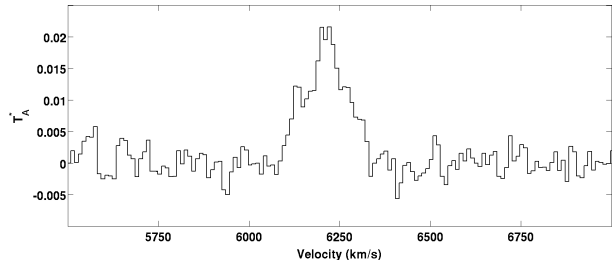


Fig. 7.— IRAM spectrum of VGS.31b in the 115.271 GHz. The intensity scale is in T_A^* , in Kelvin.

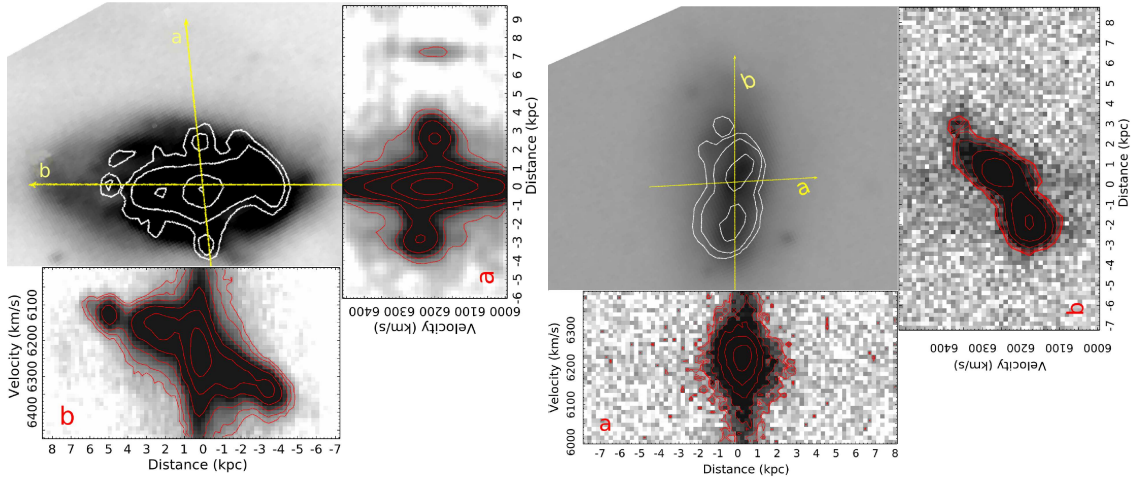


Fig. 8.— H_α major and minor axis spectra and images for VGS_31b (left) and VGS_31a (right). In the two figures above, the H_α emission line spectra along the optical major and minor axis of VGS_31b and VGS_31a are shown on the same scale as their optical images. In both figures, the optical images of the galaxies are overlaid by white H_α imaging contours. On top of these, the yellow lines indicate the positions of the slits. b represents the slit position along the optical major axis and a represents the slit position along the optical minor axis. The optical images of the galaxies and the spectra are scaled in such a way that the physical sizes of the line profiles matches with the real size of the corresponding H_α emission region within ~ 0.6 kpc. Each diagram showing optical spectra have axes of relative distance from the centre (in kpc) vs. heliocentric radial velocity (in km/s).

TABLE 3
 H_α FLUXES AND LUMINOSITIES

Galaxy	$\log[F(H_\alpha + NII)]$	$\log[[F(H_\alpha)]$	$\log[I(H_\alpha)]$	$L(H_\alpha)$ ($erg\ s^{-1}$)
VGS_31a	-12.622	-12.755	-12.304 \pm 0.076	4.7×10^{41}
VGS_31b	-12.345	-12.478	-11.913 \pm 0.104	1.16×10^{42}
VGS_31c	-13.604	-13.667	-13.527 \pm 0.019	2.8×10^{40}

NOTE.—Column 1: Galaxy name. Column 2: Measured H_α flux including NII lines. Column 3: H_α flux corrected for NII deblending. Column 4: Extinction corrected H_α flux. Column 5: H_α luminosity derived from the extinction corrected H_α flux.

TABLE 4
STAR FORMATION PROPERTIES.

Galaxy	SFR_α ($M_\odot yr^{-1}$)	SFR_{UV} ($M_\odot yr^{-1}$)	S_SFR_α ($10^{-8} M_\odot yr^{-1}$)	SFR_α/M_{HI} ($10^{-8} M_\odot yr^{-1}$)	SFR_α/M_{H_2} ($10^{-8} M_\odot yr^{-1}$)
VGS_31a	2.5	1.4	0.07	0.13	-
VGS_31b	6.3	2.2	0.06	0.43	0.7
VGS_31c	0.15	0.22	0.05	0.09	-

NOTE.—Column 1: Galaxy names. Column 2: Star formation measured from H_α flux luminosities. Column 3: Star formation calculated from NUV Column 4: Specific star formation rate. Column 5: Star formation rate per HI mass. All three galaxies have similar S_SFR_α 's while their SFR_α/M_{HI} are different.

TABLE 5
STELLAR, HI AND MOLECULAR MASSES AND CO(1-0) LUMINOSITIES FOR VGS31.

Galaxy	M_* ($10^8 M_\odot$)	M_{HI} ($10^8 M_\odot$)	L_{CO} ($10^8 \text{ K km } s^{-1} pc^2$)	M_{H_2} ($10^8 M_\odot$)	M_{H_2}/M_*	M_{H_2}/M_{HI}
VGS_31a	35.1	19.89 ± 2.90	-	-	-	-
VGS_31b	105.31	14.63 ± 1.97	2.8	8.9	0.085	0.608
VGS_31c	2.92	1.66 ± 0.95	-	-	-	-

NOTE.—Stellar masses are taken from the publicly available MPA-JHU catalog for SDSS DR7 which were derived using fits to the broad-band *ugriz* photometry. VGS31 galaxies are all spectroscopic targets in SDSS DR7 with $3''$ fiber spectra in their central regions and these spectra have been analyzed and included in this catalog.

velocity. Also the extreme ends of the filament are at the same velocities suggesting a single, coherent filamentary structure.

3.2. Kinematic properties

The kinematics along this perceived filamentary structure is, however, rather complex. We will examine this, galaxy by galaxy, going from east to west in Figure 4.

VGS_31b: The optical tail has a HI counterpart, showing almost no velocity gradient. There is a slight offset between this HI tail and its optical counterpart. It is kinematically connected to the inner disk and the ring of VGS_31b. The spatial resolution is insufficient to distinguish the gas associated with the ring from the gas associated with the disk. Therefore, we can not say whether the HI tail is connected to the inner disk or the ring. The galaxy disk and the ring exhibit rotation with a velocity spread of 325 km s^{-1} . The H_α spectrum (Figure 8) shows the rotation along the optical major axis. In the PV diagram, the velocity gradient is not as steep because the slice has not been exactly placed along the optical major axis but rather towards the tail. West of the disk, we see a HI bridge between VGS_31b and VGS_31a. Close to VGS_31b the HI in this bridge has a velocity dispersion of $\sim 50 \text{ km s}^{-1}$. In *VGS_31b*, there is almost no velocity gradient in the H_α emission along the optical minor axis whereas we see a significant gradient along the optical major axis.

VGS_31a: However, halfway to VGS_31a the velocity dispersion becomes significantly larger, $\sim 125 \text{ km s}^{-1}$. This behaviour is repeated at the other side of VGS_31a as well. The HI bridge has not been detected in the optical or UV. The gas associated with VGS_31a shows broad velocity range. However, we don't have the spatial resolution to map the HI kinematics in detail. As we move away from the galaxy towards the west, we continue to see HI with a broad velocity dispersion. The H_α spectrum (Figure 8), has much higher resolution and shows a large kinematic asymmetry.

VGS_31c: Very little HI is detected between VGS_31a and VGS_31c. A clear HI connection is however visible in Figure 4. The velocity dispersion of the HI bridge becomes again narrower as we approach VGS_31c. As for the bridge between

VGS_31b and VGS_31a, there is no stellar counterpart for this HI bridge either. The HI resolution is not enough to determine the detailed gas kinematics of VGS_31c.

3.3. Structure of the galaxies

In addition to HI, optical data complement the picture of VGS_31's complex dynamics. We will continue to describe the peculiar features of the system going from east to west.

VGS_31b: As seen from Figure 1, VGS_31b is, optically, the most disturbed galaxy. It has a one sided tail, curved towards the north east. There is a ring like structure around the disk. The tail and the disk seem to be connected. The first zoomed image shows the inner disk. The second zoomed image displays the bar positioned asymmetrically in the disk and the bright central part. The H_α emission of VGS_31b shows clear rotation along the optical major axis. In addition there is a very fast rotating inner structure, about 1 kpc in extent with a velocity width of $\sim 500 \text{ km/s}$. Along the minor axis a minor velocity difference is seen, indicative of non-circular motions along the bar (Figure 8). Also, all star formation is concentrated in this central region where the bar is present. VGS_31b has been detected in CO(1-0). The velocity of the CO(1-0) peak is at $\sim 6200 \text{ km s}^{-1}$, which is similar to the velocity of the HI.

VGS_31a: The zoom-in image (Figures 1) of VGS_31a shows that it is slightly disturbed and the bar like structure in the center overlaps with the H_α emission region (Figures 5). Like VGS_31b, rotation is along the optical major axis. However, the H_α emission line profile along the major axis is quite irregular.

VGS_31c: This is the smallest of the three galaxies without any significant morphological irregularities (Table 5). As in the other two galaxies, the star formation is confined to the central part of the disk.

3.4. Star formation properties

The H_α and UV results show that all three galaxies exhibit recent star formation activity concentrated in their central parts (Figure 5 and Table 4). The tail and the ring of VGS_31b are not detected in H_α or UV. The same is true for the HI bridges between VGS_31b, VGS_31a and

VGS_31c. Among the three galaxies, VGS_31b has significantly higher SFR_α (Table 4). We also emphasize that the small $D_n(4000)$ break values are indications for young stellar populations in the central part of the galaxies.

From the SDSS spectra we may determine the location of the VGS_31 members in a Baldwin, Phillips & Terlevich (BPT) diagram (Baldwin et al. 1981) shown in Figure 6. For this diagram, emission lines of all galaxies, including VGS_31, have been extracted from the SDSS DR7 spectral database of 3" fiber apertures. In this diagram, both VGS_31a and VGS_31b are located in the HII zone together with the other starburst galaxy samples. Their SDSS spectra have strong Balmer emission lines with large equivalent widths and blue continua. VGS_31a and VGS_31b are located inside the HII/ starburst region in the BPT diagram while VGS_31c is placed inside the normal star forming zone.

Stellar masses of the three galaxies range from $3 \times 10^8 M_\odot$ to $1.06 \times 10^{10} M_\odot$ (Table 5). In contrast to the difference in their stellar masses, they have similar S_SFR_α . It is worth noting that their S_SFR_α and $\text{SFR}_\alpha/M_{\text{HI}}$ are significantly above the median of those of the ALFALFA average density sample (Kreckel et al. 2012), indicating enhanced star formation in comparison with galaxies of similar mass and gas content.

4. Discussion

VGS_31 is a peculiar system through which we may be witnessing the ongoing growth of three galaxies along a filament inside a void. Here we discuss possible scenarios for the evolution of the VGS_31 galaxies in the void including gas accretion from an intra-void filament, interactions and merging. These processes are difficult to disentangle from one another on the basis of the observational material presented. Yet we will discuss the observed phenomena in the context of all of these processes and indicate which we consider most important in each of the individual galaxies.

First we will discuss different interaction scenarios for VGS_31a and VGS_31b using the observational results presented above. VGS_31b is the most eye-catching member in the system. A one sided tidal tail and a ring like structure are clearly visible in the optical (Figure 1). This mor-

phology suggests a minor merging incident with a low mass galaxy. A satellite galaxy could have left the tail and formed the ring by wrapping the disk of VGS_31b (Mihos & Hernquist 1994, 1996; Duc & Renaud 2011). It is less likely that the tail has been caused by tidal interaction between VGS_31b and VGS_31a. As the mass ratio of these systems is 3 to 1 one would expect greater damage to the disks and more prominent tails and counter-tail features as usually seen in tidal interactions and major mergers (Hibbard & van Gorkom 1996). The disks of VGS_31b and VGS_31a are not destroyed as expected in minor mergers (Schweizer 2000; Martínez-Delgado et al. 2010; Duc & Renaud 2011).

VGS_31b has a bar, visible in close up images in Figure 1. The bar is pronounced in H_α as well (Figure 5). The kinematics of the H_α (Figure 8) indicate a fast rotating inner structure and evidence for streaming motions characteristic for a bar. In addition, VGS_31b is a starburst Markarian galaxy having enhanced star formation in its central part overlapping with the bar (Figure 5 and 8, Table 4). The detection of CO and location of VGS_31b in the BPT diagram support the starburst picture, presumably the consequence of gas accretion into its central part as seen in many galaxy mergers and interactions (Mihos & Hernquist 1994, 1996; Duc & Renaud 2011). There is an offset between the stellar and the gas component of the tail (Figure 3). This is also observed in some tidally interacting systems (Mihos 2000) and may be due to different initial distributions of both components or additional processes that act on one component and not on the other (see Duc & Renaud 2011, for a recent review). On the other hand, in most of the tidal tails in mergers, ongoing star formation is observed (Hibbard & van Gorkom 1996; Neff et al. 2004), in the case of VGS_31b, however, no ongoing star formation has been detected neither in the tail nor in the ring (Figure 5).

VGS_31a, however, shows different characteristics. It has no visible tails, but the internal kinematics is disturbed (see the H_α kinematics in Figure 7) and the HI shows that gas east and west of the galaxy exhibits a large spread in velocity as if there is a corotating halo filled with HI rather than tidal features with simple kinematics (Figure 4). Like VGS_31b, VGS_31a is a starburst

galaxy with enhanced star formation in its central part (Figure 5 and 6, Table 4). There are two possibilities for the mechanism which could cause the enhanced star formation and the morphological disturbance: *i*) VGS_31a could be in interaction with VGS_31b and this may cause the disturbance in its morphology and results in the irregular H_α emission line profile. *ii*) Instead of accreting gas from VGS_31b, VGS_31a may experience steady gas infall from the intergalactic medium, presumably from the structure outlined by the location of the galaxies and the HI ‘connecting’ them (Figure 4). This could cause the enhanced star formation as in the first scenario and better explains the broad velocity range of the HI surrounding VGS_31a. One could argue that if VGS_31a exhibits such accretion from an LSS filament, then one would also expect VGS_31b to show the same characteristics. On the other hand it is conceivable that a minor merger, as suggested by the tail and ring could have disrupted the accretion process. Detailed simulations of such scenarios are required to test the validity of these scenarios.

VGS_31c, the smallest of the three galaxies, has enhanced star formation and its HI shows the characteristics of interactions, albeit at very low signal to noise. It is difficult in this case to determine conclusively the process(es) responsible for the HI structure and enhanced star formation.

The most exciting result is that we may be witnessing the assembly of structure within a void, and the birth process of galaxies in such a desolate area. It does fit into the theoretically expected buildup of voids and galaxies therein. Voids evolve in a hierarchical fashion, leaving planar and filamentary substructure within the emerging voids (Dubinski et al. 1993; van de Weygaert & van Kampen 1993; Sahni et al. 1994; Sheth & van de Weygaert 2004; Aragón-Calvo & Szalay 2013) and (Rieder et al. 2013 (subm.)). The question is whether we see here the manifestation of this process. VGS_31 could be a density enhancement within an underlying dark matter filament. The complication is that in addition to accretion of material from a LSS filament the galaxies also suffer from tidal interactions and minor merging. As for the cold flow accretion scenarios we can only make a very rough estimate because we don’t know exactly the orientation of the system. If we take the size of the HI filament and the velocity gradient

from east to west then we can estimate a rough accretion timescale of at least a gigayear. An important next step will be to use advanced simulations with gas and star formation to see whether the scenario proposed here does indeed take place in voids.

Finally, it is of interest to note that VGS_31 is not the only case for a filamentary structure and cold flow accretion in our Void Galaxy Survey. We have discovered at least two other cases which seem to exhibit this hierarchical structure formation. In addition to another filamentary galaxy configuration, VGS_38 (Kreckel et al. 2011), we also found a polar disk galaxy, VGS_12 (Stanonik et al. 2009). VGS_38 is a system of chain galaxies which share the same HI. VGS_12 is located right at the center of a tenuous wall between two large voids. It has a polar HI disk much more extended than its stellar disk. The polar disk has no stellar counterpart or any ongoing star formation. This galaxy is a candidate for the cold flow accretion.

Individually these galaxies and VGS_31 are unusual systems, however taken collectively they show that the void environment is an extremely interesting site for understanding galaxy formation and evolution.

Acknowledgments

We wish to thank the anonymous referee for interesting and helpful comments. RvdW and BB are grateful to Steven Rieder and Marius Cautun for many helpful discussions and insightful thoughts. BB wishes to thank Reynier Peletier for his help in spectral analysis and the staff of the IRAM observatory for their tremendous help in conducting our observations and IGN (Spain). This work was supported in part by the National Science Foundation under grant no. 1009476 to Columbia University. We are grateful for support from Da Vinci Professorship at the Kapteyn Institute. The Isaac Newton Telescope and The William Herschel Telescope are operated on the island of La Palma by the Isaac Newton Group in the Spanish Observatorio del Roque de los Muchachos of the Instituto de Astrofísica de Canarias. MDM observatory is located on the southwest ridge of Kitt Peak, home of the Kitt Peak National Observatory, Tucson, Arizona. The Observatory is owned and operated by a consortium

of five universities: the University of Michigan, Dartmouth College, the Ohio State University, Columbia University, and Ohio University. We acknowledge KPNO for the use of their H α filters. The Westerbork Synthesis Radio Telescope is operated by the ASTRON (Netherlands Institute for Radio Astronomy) with support from the Netherlands Foundation for Scientific Research (NWO). IRAM is supported by INSU/CNRS (France), MPG (Germany) and has benefited from research funding from the European Community's Seventh Framework Programme.

REFERENCES

- Aragón-Calvo, M. A., Platen, E., van de Weygaert, R., & Szalay, A. S. 2010a, *ApJ*, 723, 364
- Aragón-Calvo, M. A., & Szalay, A. S. 2013, *MNRAS*, 428, 3409
- Aragón-Calvo, M. A., van de Weygaert, R., & Jones, B. J. T. 2010b, *MNRAS*, 408, 2163
- Baldwin, J. A., Phillips, M. M., & Terlevich, R. 1981, *PASP*, 93, 5
- Bond, J. R., Kofman, L., & Pogosyan, D. 1996, *Nature*, 380, 603
- Calzetti, D., Armus, L., Bohlin, R. C., Kinney, A. L., Koornneef, J., & Storchi-Bergmann, T. 2000, *ApJ*, 533, 682
- Ceccarelli, L., Padilla, N. D., Valotto, C., & Lambas, D. G. 2006, *MNRAS*, 373, 1440
- Colberg, J. M., Krughoff, K. S., & Connolly, A. J. 2005a, *MNRAS*, 359, 272
- Colberg, J. M., Sheth, R. K., Diaferio, A., Gao, L., & Yoshida, N. 2005b, *MNRAS*, 360, 216
- Colless, M., et al. 2003, *ArXiv Astrophysics e-prints*
- Costagliola, F., et al. 2011, *A&A*, 528, A30
- Coziol, R. 2003, *MNRAS*, 344, 181
- Davis, M., Huchra, J., & Latham, D. 1983, in *IAU Symposium, Vol. 104, Early Evolution of the Universe and its Present Structure*, ed. G. O. Abell & G. Chincarini, 167–172
- Domínguez, A., et al. 2012, *ArXiv e-prints*
- Dubinski, J., da Costa, L. N., Goldwirth, D. S., Lecar, M., & Piran, T. 1993, *ApJ*, 410, 458
- Duc, P.-A., & Renaud, F. 2011, *ArXiv e-prints*
- Einasto, J., et al. 2011, *A&A*, 534, A128
- Furlanetto, S., & Piran, T. 2006, *MNRAS*, 366, 467
- Gavazzi, G., Boselli, A., Cortese, L., Arosio, I., Gallazzi, A., Pedotti, P., & Carrasco, L. 2006, *A&A*, 446, 839
- Gottlöber, S., Lokas, E. L., Klypin, A., & Hoffman, Y. 2003, *MNRAS*, 344, 715
- Grogin, N. A., & Geller, M. J. 1999, *AJ*, 118, 2561
- . 2000, *AJ*, 119, 32
- Hibbard, J. E., & van Gorkom, J. H. 1996, *AJ*, 111, 655
- Hoyle, F., & Vogeley, M. S. 2002, *ApJ*, 566, 641
- Hoyle, F., Vogeley, M. S., & Gott, III, J. R. 2002, *ApJ*, 570, 44
- Huchra, J. P., et al. 2012, *ApJS*, 199, 26
- Karachentseva, V. E., Karachentsev, I. D., & Richter, G. M. 1999, *A&AS*, 135, 221
- Kennicutt, Jr., R. C., Lee, J. C., Funes, José G., S. J., Sakai, S., & Akiyama, S. 2008, *ApJS*, 178, 247
- Kennicutt, Jr., R. C., et al. 2009, *ApJ*, 703, 1672
- Kreckel, K., Platen, E., Aragón-Calvo, M. A., van Gorkom, J. H., van de Weygaert, R., van der Hulst, J. M., & Beygu, B. 2012, *AJ*, 144, 16
- Kreckel, K., et al. 2011, *AJ*, 141, 4
- Kroupa, P., & Weidner, C. 2003, *ApJ*, 598, 1076
- Kuhn, B., Hopp, U., & Elsaesser, H. 1997, *A&A*, 318, 405
- Martínez-Delgado, D., et al. 2010, *AJ*, 140, 962
- Massey, P., Strobel, K., Barnes, J. V., & Anderson, E. 1988, *ApJ*, 328, 315
- Mihos, C. 2000, *ArXiv Astrophysics e-prints*

- Mihos, J. C., & Hernquist, L. 1994, *ApJ*, 425, L13
— . 1996, *ApJ*, 464, 641
- Neff, S. G., et al. 2004, in *Bulletin of the American Astronomical Society*, Vol. 36, American Astronomical Society Meeting Abstracts, 1385
- Oke, J. B. 1990, *AJ*, 99, 1621
- Patiri, S. G., Betancort-Rijo, J. E., Prada, F., Klypin, A., & Gottlöber, S. 2006a, *MNRAS*, 369, 335
- Patiri, S. G., Prada, F., Holtzman, J., Klypin, A., & Betancort-Rijo, J. 2006b, *MNRAS*, 372, 1710
- Peebles, P. J. E. 2001, *ApJ*, 557, 495
- Platen, E., van de Weygaert, R., & Jones, B. J. T. 2007, *MNRAS*, 380, 551
- Popescu, C. C., Hopp, U., & Elsaesser, H. 1997, *A&A*, 325, 881
- Portegies Zwart, S., et al. 2010, *IEEE Computer*, v.43, No.8, p.63-70, 43, 63
- Raimann, D., Storchi-Bergmann, T., Bica, E., Melnick, J., & Schmitt, H. 2000, *MNRAS*, 316, 559
- Rojas, R. R., Vogeley, M. S., Hoyle, F., & Brinkmann, J. 2004, *ApJ*, 617, 50
— . 2005, *ApJ*, 624, 571
- Sahni, V., Sathyaprakah, B. S., & Shandarin, S. F. 1994, *ApJ*, 431, 20
- Saintonge, A., et al. 2011, *MNRAS*, 415, 32
- Schaap, W. E., & van de Weygaert, R. 2000, *A&A*, 363, L29
- Schiminovich, D., et al. 2010, *MNRAS*, 408, 919
- Schweizer, F. 2000, in *Royal Society of London Philosophical Transactions Series A*, Vol. 358, Astronomy, physics and chemistry of H^+_3 , 2063
- Shandarin, S. F., & Zeldovich, Y. B. 1989, *Reviews of Modern Physics*, 61, 185
- Sheth, R. K., & van de Weygaert, R. 2004, *MNRAS*, 350, 517
- Springel, V., Frenk, C. S., & White, S. D. M. 2006, *Nature*, 440, 1137
- Stanonik, K., Platen, E., Aragón-Calvo, M. A., van Gorkom, J. H., van de Weygaert, R., van der Hulst, J. M., & Peebles, P. J. E. 2009, *ApJ*, 696, L6
- Szomoru, A., van Gorkom, J. H., Gregg, M. D., & Strauss, M. A. 1996, *AJ*, 111, 2150
- Terlevich, R., Melnick, J., Masegosa, J., Moles, M., & Copetti, M. V. F. 1991, *A&AS*, 91, 285
- Tikhonov, A. V., & Karachentsev, I. D. 2006, *ApJ*, 653, 969
- van de Weygaert, R., & Platen, E. 2011, *International Journal of Modern Physics Conference Series*, 1, 41
- van de Weygaert, R., & Schaap, W. 2009, in *Lecture Notes in Physics*, Berlin Springer Verlag, Vol. 665, Data Analysis in Cosmology, ed. V. J. Martínez, E. Saar, E. Martínez-González, & M.-J. Pons-Bordería, 291–413
- van de Weygaert, R., & van Kampen, E. 1993, *MNRAS*, 263, 481
- Wegner, G., & Grogin, N. A. 2008, *AJ*, 136, 1
- York, D. G., et al. 2000, *AJ*, 120, 1579
- Zel'dovich, Y. B. 1970, *A&A*, 5, 84
- Zitrin, A., & Brosch, N. 2008, *MNRAS*, 390, 408

This 2-column preprint was prepared with the AAS L^AT_EX macros v5.2.